Applicability of the VisiSize D30 shadowgraph system for cloud microphysical measurements

Jakub L. Nowak[1,*], Moein Mohammadi[1,*], and Szymon P. Malinowski[1]

[1]Institute of Geophysics, Faculty of Physics, University of Warsaw, Warsaw, 02-293, Poland
[*]These authors contributed equally to this work.

Correspondence: Jakub L. Nowak (jakub.nowak@fuw.edu.pl)

Abstract. The commercial shadowgraph system, Oxford Lasers VisiSize D30, originally designed to characterize industrial and agricultural sprays, was tested with respect to the application for measuring cloud microphysical properties, such as droplet size distribution and number concentration. Laboratory experiment with a dense stream of poly-disperse cloud-like droplets indicated strong dependence of the depth of field, thus also sample volume, on particle size. This relationship was determined and a suitable correction method was developed to improve estimations of droplet number concentration and size distribution. Spatial homogeneity of detection probability inside the sample volume and minimum droplet diameter providing uniform detection were examined. The second experiment with mono-disperse droplets produced by Flow-Focusing Monosized Aerosol Generator (FMAG) verified sizing accuracy and demonstrated reasonable agreement between the instruments. Effects of collisions and evaporation of droplets produced by FMAG were observed. Finally, the instrument was applied to sample atmospheric clouds at a ground-based mountain observatory and performed reliably during 3 week long field experiment. Based on the laboratory and field tests, recommendations concerning the use of the instrument for cloud droplet measurements were formulated.

1 Introduction

Atmospheric clouds predominantly consist of water droplets. Cloud droplet number concentration (DNC) and size distribution (DSD) constitute the key parameters for quantitative microphysical description of clouds and attract enormous attention in contemporary atmospheric sciences, mostly due to their crucial importance for cloud lifetime, radiative effects and rain formation (Devenish et al., 2012).

There exist two general approaches to measuring cloud microphysical properties: in situ sampling from airborne platforms or at ground-based stations and remote sensing which involves applying inverse retrieval techniques to data collected by satellites, radars and radiometers. Researchers employing both strategies tackle with intrinsic difficulties. For instance, in situ methods often face the dependence of the sample volume on particle size or air flow velocity, nonlinearity of the Mie scattering intensity with respect to droplet size, aerodynamic effects related to the flow around or inside the instrument or aircraft, harsh conditions (incl. icing, wetting, temperature changes), necessity for handling large datasets or instantaneous data processing. Remote sensing provides the information with limited spatial resolution, hence microphysical properties represents only the average or integral over relatively large volumes which might be too simplistic to characterize inhomogeneous or multi-layered cloud

25 fields. On top of that, the retrievals are often dependent on the assumptions of specific size distribution or specific vertical structure of the atmosphere. In general, in situ measurements are considered fundamental, as they offer instrumental access to individual droplets within a sampling volume. The results obtained in situ are then used to derive and validate inversion routines to be used in remote sensing applications.

Among in situ techniques, one can distinguish two branches differing in sampling style:

30 – instruments detecting and counting droplets one-by-one but almost continuously in time as they pass through a very small active probe volume provide individual droplet properties and their inter-arrival times,

– instruments capturing images or other spatial representation of droplets inside a larger sampling volume provide individual droplet properties and information on their spatial arrangement.

The first branch is represented by a number of spectrometers using light scattering for droplet detection and sizing, e.g. For-
35 ward Scattering Spectrometer Probe (FSSP, e.g. Cooper (1988); Brenguier et al. (1998); Gerber et al. (1999); de Araújo Coelho et al. (2005)), Cloud Droplet Probe (CDP, e.g. McFarquhar et al. (2007); Lance et al. (2010); Lance (2012)), Cloud and Aerosol Spectrometer (CAS, e.g. Lance (2012); Glen and Brooks (2013); Barone et al. (2019)), Phase Doppler Interferometer (PDI, e.g. Bachalo and Houser (1984); Chuang et al. (2008); Kumar et al. (2019)). In practice, they sample quasi one-dimensional portion of air passing through the region of active sampling. The exact volume sampled in unit time depends on the velocity
40 with respect to the instrument. Therefore, meaningful estimation of DNC requires information on air velocity. Moreover, due to small probe volume cross-section, there exist an upper limit for measurable droplet size. For instance, the range of diameters of the CDP equals 2-50 μm.

Volumetric methods (second branch) usually do not rely on scattering intensity of individual droplet in sizing and their sampling volumes do not depend on the velocity of the flow but consecutive air samples, collected instantaneously, might be
45 quite distant from each other, in particular when used on fast moving airborne platforms. This class of techniques is represented e.g. by shadowgraphy and holography. Neglecting the effect of imperfect focusing, shadow image constitutes two-dimensional projection of all the objects onto camera plane and can be rapidly processed to detect particles and obtain relevant statistics. Holograms require extensive processing to digitally reconstruct objects' shape and arrangement in three dimensions (Fugal et al., 2009). Both methods allow to study position, size and shape, thus not only spherical droplets but also e.g. ice crystals.
50 Holographic systems have been successfully deployed on research aircrafts (HOLODEC, Fugal and Shaw (2009), and HALOHolo, Schlenczek et al. (2017), Schlenczek (2017), Lloyd et al. (2020)), ground-based mountain observatories (HOLIMO, Henneberger et al. (2013)), mountain cable cars (HoloGondel, Beck et al. (2017)) and balloon-borne platforms (HoloBalloon, Ramelli et al. (2020)). Typically, those instruments have resolution of 6 μm, sample volume (SV) of about 15 cm^3 and take a few holograms per second which results in the sample volume rate (SVR) of around 90 $\mathrm{cm}^3\,\mathrm{s}^{-1}$. The recent HoloBallon setup
55 features SV of 22.5 cm^3 and frame rate of 80 fps which gives SVR of 1800 $\mathrm{cm}^3\,\mathrm{s}^{-1}$. Shadowgraphy has been used e.g. in Cloud Particle Imager (CPI, Lawson et al. (2001), Connolly et al. (2007)), an airborne instrument to observe ice particles and supercooled droplets in the size range of 2.3-2300 μm (Woods et al., 2018). Typical SV is much smaller than in holography (about 0.04 cm^3), however the frames rate is much higher (400 fps) which gives the SVR of about 16 $\mathrm{cm}^3\,\mathrm{s}^{-1}$. Moreover,

Rydblom and Thörnberg (2016) have designed a system to investigate icing conditions for wind turbines based on shadow images. Nevertheless, despite both its simplicity and many insightful laboratory experiments, e.g. concerning droplet collisions (Bordás et al., 2013; Bewley et al., 2013), shadowgraphy is not the first choice method in cloud droplet measurements.

In order to explore in detail the advantages and disadvantages of shadowgraphy for cloud microphysical applications, we use the commercial shadowgraph system (VisiSize D30, Oxford Lasers Ltd., Kashdan et al. (2003, 2004)), originally designed for diagnosis of agricultural and industrial sprays, to measure DNC and DSD in warm clouds. Within the study, two series of laboratory experiments were performed which aimed at verifying reliability of detection and accuracy of sizing under conditions resembling atmospheric clouds. They were followed by a field experiment targeting real cloud at a mountaintop observatory.

The present paper is structured as follows. Section 2 describes the instrument and the measurement principle. Section 3 provides the analysis of detection reliability and homogeneity affecting results on DNC and DSD, investigated with the use of poly-disperse water droplets. Section 4 focuses on sizing accuracy studied with the use of mono-disperse droplet population. Based on the experiments, corrections to the standard algorithm implemented in instrument software are suggested. Finally, in section 5 we present selected results obtained during the first application of the instrument in atmospheric clouds. The last section summarizes the findings and discusses the conclusions concerning the further usage of the VisiSize D30 system for cloud research.

2   System overview

VisiSize D30 is a complete shadowgraph system manufactured by Oxford Lasers Ltd. (Oxon, United Kingdom) designed to characterize particles in various suspensions. Common industrial applications include among others the characterization of: agricultural sprays, paint sprays, consumer aerosols, fire extinguishers and automotive fuel injectors.

2.1   Hardware description

The two main parts of the set-up are infrared diode pulse laser with diffuser and digital camera with suitable lens objective (see Fig. 1). Lens magnification can be changed manually to adjust the resolution and extent of the sample volume to the object of study. For three selected options, instrument calibration was performed by the supplier. Capabilities of the system at those settings are listed in Table 1.

The operation of the system is the following. The region of interest is illuminated from behind by diffused (incoherent) expanded laser light beam, then shadow images of droplets are collected at up to 30 frames or pairs of frames per second with a digital camera. The laser and the camera are jointly triggered so that a single laser pulse "freezes" the motion of droplets present within the measurement volume during each frame capture. Droplets detected inside the depth of field (DOF) are then measured based on their shadow images, and statistics regarding concentration or size distribution are built by processing a series of images. Worth to mention, there is also an option to measure droplet velocity in the imaging plane by comparing pairs of consecutive frames and measuring droplet displacement between them. The captured images are either processed in
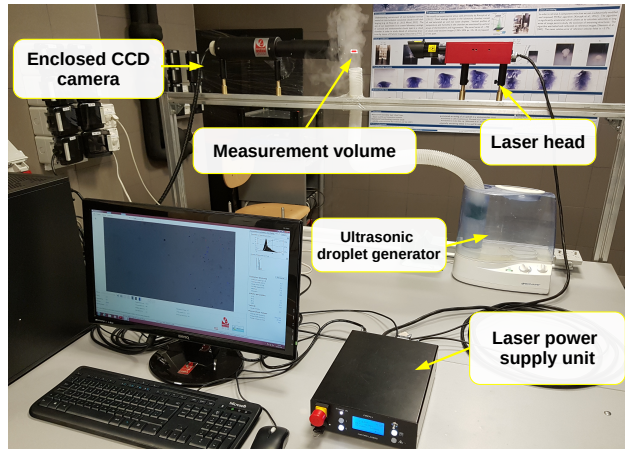
Figure 1. Experimental setup for studying detection properties (see sec. 3 for details). Main parts of the VisiSize D30 are: infrared pulse laser with a diffuser (top-right), CCD camera with lens objective enclosed in a water-proof housing (top-left). Water droplets produced with an ultrasonic droplet generator are measured while passing through the sample volume (top-middle) located close to the camera.

Table 1. Properties of the VisiSize D30 system for three different lens magnification settings provided by Oxford Lasers Ltd.

VisiSize D30 specifications			
Camera chip [pix x pix]	1952 x 1112		
Camera pixel [µm]	5.5		
Frame rate [fps]	30		
Wavelength [nm]	808		
Laser pulse duration [µs]	0.1 - 5.0		
Lens setting	x1	x2	x4
Magnification	1.49	2.97	6.12
Effective pixel size [µm]	3.69	1.85	0.90
Resolution [µm]	6.9	3.7	2.0
Field of view [mm x mm]	7.20 x 4.10	3.62 x 2.06	1.75 x 1.00
Depth of field [mm]	50.0	16.6	5.2
Sample volume [cm^3]	1.48	0.123	0.0092
Volume rate [$cm^3\,s^{-1}$]	44.3	3.71	0.28

real-time to determine particle positions and sizes (live mode) or stored as graphic files (capture mode). In case of the former, the output is only a list of particles together with their properties (droplet file). Specific quantities included in the droplet file are explained in Table 2. The second complementary output file contains system settings used and measurement summary with

some basic statistics of the recorded droplet set (summary file). For the capture mode, one can analyse captured images later
tuning some parameters or access the raw genuine view of the particles (see Fig. 3 in sec. 3.1). However, then the total time of
uninterrupted measurement is limited by available computer RAM.

Table 2. Explanation of the parameters reported in output droplet file together with corresponding symbols used to denote them in the text.

Parameter	Symbol	Units	Description
Frame	j	-	Number of the image containing current particle
Particle ID	i	-	Particle number, unique across dataset
Area	A	μm^2	Estimated cross-sectional area, calculated from D
Diameter	D	μm	Estimated particle diameter, calculated based on A_p and A_h
Shape Factor	S_f	-	Measure of sphericity equal to the ratio of the principle moments of inertia of the shadow, taking values from 0 to 1, with 1 representing a perfect circle
X	x	pix	Horizontal position in camera plane
Y	y	pix	Vertical position in camera plane
Pixel Area	A_p	pix^2	Number of pixels in particle shadow with brightness below threshold T_p
Pixel Halo	A_h	pix^2	Number of pixels in particle shadow with brightness between thresholds T_h and T_p where $T_h < T_p$
Distance to Focal Plane	z	μm	Estimated axial position in the sample volume, calculated based on A_p and A_h; insensitive to direction, thus always positive

2.2 Principle of droplet detection and sizing

The measurement principle applied in VisiSize system was explained by Kashdan et al. (2003, 2004). It stems from the basic
observation that with increasing defocus (particle displacement out of the focal plane of the camera lens) the image of the
object is more and more blurred which hinders the proper estimation of the size of the shadow. On the other hand, the range
of axial positions guaranteeing acceptable sharpness of the shadow is usually quite limited. As a consequence, the probability
of detecting particle inside such restricted SV might be often insufficient to collect meaningful statistics of the suspension in
reasonable time. To overcome difficulties described above, Kashdan et al. (2003) applied a method compensating for the effects
of imperfect focus. Basically, the displacement from the focal plane is estimated from the degree of image blurring, specifically
the gradient of brightness at the edge of inner dark shadow. In their implementation, two threshold limits are determined for
each analysed picture based on the histogram of pixel brightness. Both of them lie between the background intensity and the
level corresponding to dark centers of particle shadows (see Fig. 2). The upper threshold T_p separates the background from the
particle image. All pixels below this value are assumed to belong to effective total particle image area A_p (with the equivalent
diameter D_p). The lower threshold T_h distinguishes between the dark shadow interior and an outer gray "halo". Pixel with

intensities between T_h and T_p are counted to produce the estimate of particle halo area A_h (with the equivalent width D_h). Therefore, A_h belongs to A_p and has to be smaller.
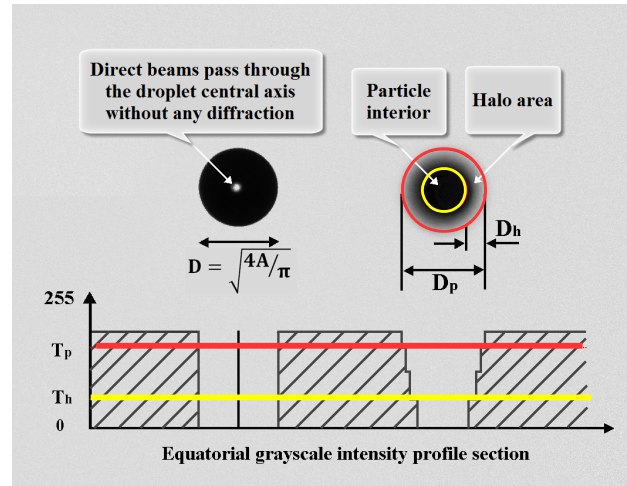
Figure 2. Schematic representation of threshold method showing shadow image of two sample droplets, in-focus droplet (left) and defocused droplet (right), alongside grayscale intensity profiles below them illustrating applied thresholds.

With increasing defocus distance, the total area of particle image grows due to blurring until at some point it fades away into background making the object no longer distinguishable. Worth to mention, halo area A_h grows faster than total area A_p because it extends both into outer and inner direction, taking over respectively the background and the interior pixels. Ideally, for object standing exactly in the focal plane A_h should tend to zero. However, it is never the case due to intrinsic diffraction caused by finite aperture of the lens. This effect might be particularly important for small object of the size close to the optical resolution of the system.

Particle total area A_p and halo area A_h can be regarded as directly measured quantities. Both true particle diameter D and estimated defocus distance z are derived from them. The exact conversion is determined with experimental calibration, separately for each lens setting. The pictures of calibration targets of known sizes are taken at known distances away from the focal plane. Applying the sizing algorithm to the collected data, some function is fitted to approximate the relationship $A_p(D, z)$ and $A_h(D, z)$. For the present VisiSize D30 model, calibration was performed by Oxford Lasers for three possible lens magnification settings (x1, x2 and x4) and incorporated into the software.

In principle, for perfect focusing the halo area A_h should tend to zero, since then the image consists only of a dark disk with sharp edge around. Certainly A_h grows with the distance between actual particle position and the focal plane. The halo is formed exactly around the dark interior of the shadow, i.e. each point on an initially very sharp edge spreads equally in all directions, smoothing the intensity gradient and creating halo of area which scales with the perimeter length and the amount of defocus. For objects with shape close to a circle, the perimeter is proportional to the diameter which leads to a scaling $A_h \sim Dz$. However, even a point source, while being out of the focal plane is mapped to a circle of confusion in image plane

(camera chip). Therefore A_h should be growing function of z even in case of size D tending to zero. The simple linear relation satisfying the above properties is:

$$A_h = a_1 D z + a_2 z \tag{1}$$

where a_1 and a_2 are calibration constants for a given lens magnification.

As described above, with increasing defocus distance z, halo around the dark interior develops at the cost of both the background pixels and the inner shadow pixels. The whole A_h is included in total particle pixel area A_p, so only the outward growth affects the value of A_p. Outward part of the shell is larger than inward one, hence the proportionality factor would be close to but slightly higher than 0.5. Obviously, in focal plane the image area is dependent on the true cross-section of the physical object, but A_p is composed of pixels of finite size which disturbs the perfect representation of smooth shapes. Consequently, effective diameter length might be diminished by the amount of the order of pixel size. Moreover, even for the focal plane diffraction comes into play and hinders perfect imaging - objects always appear slightly larger than in reality which is important especially for small droplets. The enlargement of diameter due to diffraction should be of the order of the optical resolution of the lens system. All the effects can be taken into account in the formula of the form:

$$A_p = a_3 A_h + \frac{\pi}{4} \frac{(D + a_4 + a_5)^2}{\text{pix}^2} \tag{2}$$

where the constants a_3, a_4, a_5 and pix describe halo blurring, pixelization, diffraction and effective pixel size, respectively. Note that A_p is specified as the number of pixels, hence the unit conversion factor pix^2 is needed. Having the values of A_h and A_p obtained from the image of the specific particle, both the diameter D and the defocus distance z can be calculated by inverting Eqs. (1) and (2).

3 Detection properties

3.1 Diagnostic experiment

First diagnostic laboratory experiment was carried out to characterize instrument performance in terms of detection probability and homogeneity which affect statistics of DNC and DSD. A dense stream of poly-disperse water droplets was generated with the use of an ultrasonic humidifier, the same as in the study of Korczyk et al. (2012) who measured the droplet size to be mostly in the range of 2-20 μm in diameter (Fig. 1 there). Differences in delivery method and in ambient conditions could result in a little different spectrum. In our setup, the cloud of droplets was delivered from the humidifier into the SV with 4 cm wide, 70 cm long circular plastic pipe. Care was taken to fill the whole shadowgraph SV with the stream of droplets though both the flow and the particle field were not exactly homogeneous. The flow velocity was estimated to be of the order of $10 \, \text{cm} \, \text{s}^{-1}$ and the direction of the flow was aligned horizontally from left to right (i.e. the direction of the pipe exit was perpendicular to what is shown in Fig. 1). For each of the three lens settings (x1, x2, x4) laser power was adjusted to reach optimal background brightness of the pictures and 10 min long measurement in live mode was performed. Figure 3 presents an example image captured during the experiment. Statistics reported by the software for each run are listed in Table 3.

Table 3. Statistics of the laboratory experiment with poly-disperse droplets for different lens magnification settings.

Lens setting	x1	x2	x4
Video frames	17705	17670	17695
Empty frames	3390	4508	8156
Total counts	602232	951642	324625
Counts/frame	34.0	53.9	18.3
Min. diameter [µm]	7.9	4.6	3.2
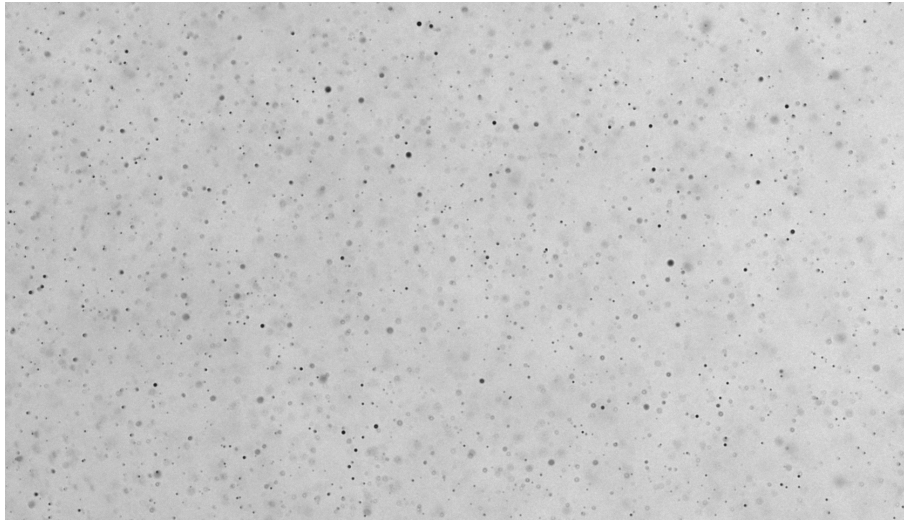
Figure 3. A typical shadow image of droplets produced by ultrasonic droplet generator taken during laboratory tests with the camera lens magnification x2.

3.2 Focus rejection and depth of field

Results of the experiment show that both halo A_h and total particle area A_p cannot take any values but their admissible range is limited by certain conditions (see Fig. 4). At sufficiently large distance away from the focal plane particle image starts to fade away into background making it no longer distinguishable. Simultaneously, halo takes over almost whole particle image. To avoid measuring objects whose signal-to-noise ratio does not allow for proper sizing, a simple rejection limit is exercised by the software:

$$A_h < 0.95 A_p \tag{3}$$

Importantly, deactivation of this option is not available from the level of the user in the software version 6.5.39.

The condition poses an upper limit for the range of values A_h can take. On the other side, the minimum halo area can be estimated by the diffraction on particle edge because diffraction effects cannot be avoided even in case of the perfect in-focus placement. Indeed, the product of the perimeter length πD times diffraction constant a_5 approximates the lower limit for halo well (see Fig. 4). Note the large values of A_h are attained only by relatively large droplets and at far defocus. Accordingly, for a given diameter the range of total particle area A_p is also limited. It can grow with defocus distance z, but only to the point where halo constitutes 95 % of the image. Otherwise, such particle would have been rejected.
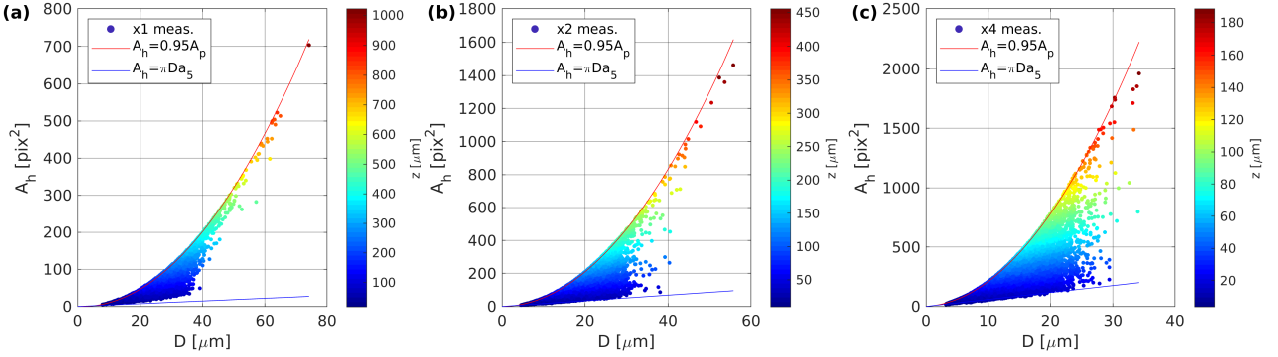
Figure 4. Range of halo areas A_h observed in measurement results with changes in diameter size D and defocus distance z for different lens magnification setting: (a) x1, (b) x2, (c) x4.

According to Eq. (1) and (2) halo grows linearly with droplet diameter while total image area grows quadratically. It means that for a given defocus distance z, halo should constitute larger fraction of the whole image for small droplets in comparison to the large ones. With increasing z the halo would fill the image much sooner in case of small objects and their shadows would sooner fade away into background, making them no longer detectable. Such qualitative reasoning explains the intuitive fact that the range of distance z within which the object can be detected depends on the object size. For instance, effective SV depends on cloud droplet diameter with all the adequate consequences for measuring DSD.

Kashdan et al. (2003) showed that, to a reasonable accuracy, the range of possible defocus distance (depth of field, DOF) $[-z_{def}, +z_{def}]$, grows linearly with particle diameter. The proportionality factor comes from the experimental calibration. The measurement volume V is then equal to the product of the default DOF z_{def} and effective area of camera sensor S (field of view, FOV).

$$z_{def} = a_6 D \qquad V = 2a_6 DS \tag{4}$$

In a summary file generated by the software, this formula is applied to calculate the volumes V_k corresponding to the consecutive size bins $[D_k, D_{k+1})$, where integers $k = 1, 2, ..., K$ denote bin number.

However, the volumes calculated with such a method are not correct for small particles as typical droplets in atmospheric clouds. The reason for this fact is that the focus rejection condition ($A_h < 0.95A_p$) impose a limitation on the acceptable defocus distance z. Hereafter this limit will be denoted z_{95}, in contrast to previously introduced z_{def}. Specific value can be

obtained by using Eq. (1) and (2) to expand inequality of the focus rejection criterion in Eq. (3).

$$z < z_{95} = \frac{0.95}{(1 - 0.95a_3)(a_1 D + a_2)} \frac{\pi}{4} \frac{(D + a_4 + a_5)^2}{\text{pix}^2} \tag{5}$$

The effect of the above condition is illustrated in Fig. 5. Indeed, for all the droplets measured in the diagnostic experiment, Eq. (3) leads to much stronger limitation of the effective SV than Eq. (4). Predicted ranges of defocus distance agree very

195 well with maximum values z_{max} found in the experimental dataset. The discrepancy observed for largest sizes is related to the poor statistics, i.e. small number of counts of large droplets which are infrequent in the measured plume. It can be shown, that focus rejection defines the true SV for particles of small diameter whereas it usually has no effect in the case of large particles like rain drops (then $z_{95} > z_{def}$). The exact critical size depends on the lens settings and the respective calibration. When one considers the relative difference between the two values it can be calculated that it drops below 10 % for particles larger than

200 210, 260 and 50 µm for lens settings x1, x2 and x4, respectively. Considering the population of such droplets, the choice of the DOF limit would have only minor effect on the results.
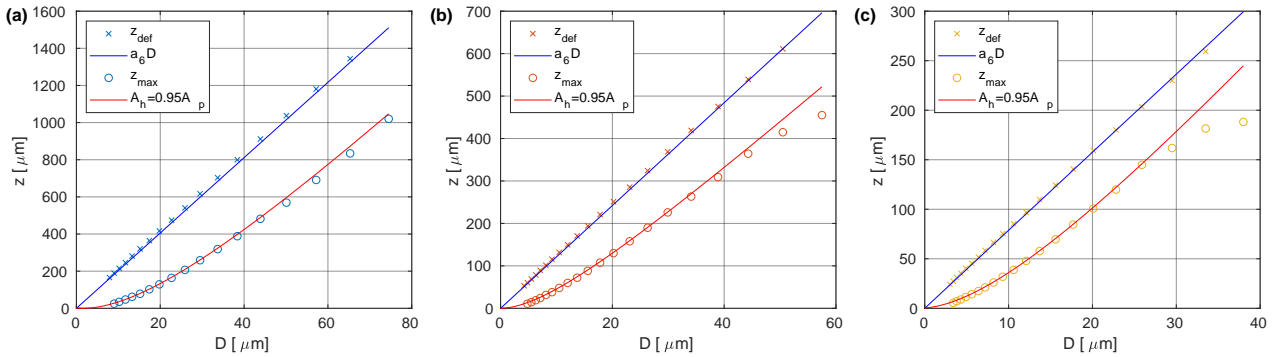
Figure 5. Maximum range of defocus distance z for each size bin: derived from the volumes listed in summary file (crosses), and the actual maximum values z_{max} found in the experimental data (circles), together with two analytical approximations - default z_{def} and corrected z_{95}. Measurement series for lens magnification settings: (a) x1, (b) x2, (c) x4.

3.3 Effective sample volumes

Size-dependent DOF has to be accounted for while calculating DSD based on shadowgraph images. Moreover, image processing procedure includes border rejection mechanism which excludes all the objects touching the outer edge of the picture

205 because sizing of such objects would be strongly biased. Thus, the effective cross-sectional area of camera sensor, FOV, is reduced by the margin of the width equal to a diameter under consideration. Cloud droplets are orders of magnitude smaller than the whole FOV, therefore such correction, although reasonable, would not exert much influence on the final results and often might be neglected. Yet, it is significant for large drops, i.e. rain. Eventually, the *default* SVs in calculations of DSD are:

$$V_k^{def} = 2z_{def} \big|_{D_k} (L_x - D_k)(L_y - D_k) \tag{6}$$

210 where L_x and L_y denote the size of the FOV in μm and k is the number of a size bin.

However, as explained above the default solution does not account for DOF limitation due to the focus rejection condition. Hence, the *corrected* SVs can be defined as follows.

$$V_k^{cor} = 2z_{95}\,|_{D_k}\,(L_x - D_k)(L_y - D_k) \tag{7}$$

If the total number of bins K is small or the spread of droplet diameters present in a dataset is particularly large, then the
215 range of sizes for objects belonging to one bin might be significant. For that reason, it would be sensible to introduce SV prescribed exactly for the particular droplet of interest. The method of calculating DSD with the use of *individual* volumes should be more precise from the physical point of view. On the other hand, it requires the access to the list of all droplets whereas corrected and default methods need only the accumulated number of particles within the bins.

$$V_i^{ind} = 2z_{95}\,|_{D_i}\,(L_x - D_i)(L_y - D_i) \tag{8}$$

220 According to the above discussion, the effect of choosing different maximum range of defocus distance on effective SV around a droplet is shown schematically in Fig. 6.
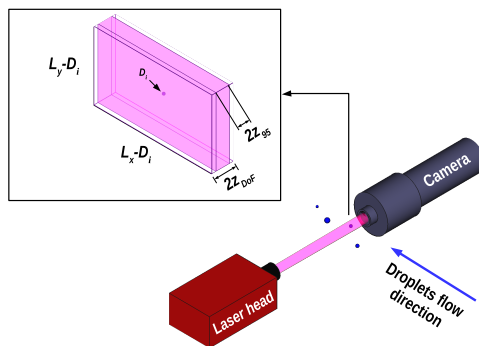
Figure 6. Schematic illustrating the difference between the default and the corrected/individual sample volume having the same field of view, $S = (L_x - D_i)(L_y - D_i)$, but differing in depth of field (z_{def} vs. z_{95}).

3.4 Correction to concentration and size distribution

Proper quantitative measures of particle concentration and distribution of their sizes in a given suspension should allow for meaningful comparisons between the measurement series, different instruments and experimental conditions. As explained, ef-
225 fective SVs depend on object sizes. Additionally, practical choice of size bins usually involves widths growing with increasing diameter. In order to characterize droplet spatial arrangement and size differentiation, we introduce a number of counts normalized with respect to both spatial position and size, denoting it as $N_{VD}(x, y, z, D)$. This quantity has units of $\mathrm{mm}^{-3}\,\mu\mathrm{m}^{-1}$

and should be interpreted as local probability density function (PDF) of droplet diameter at point (x, y, z) normalized to sum up to local total droplet concentration (number in a unit volume, DNC) at this point. Then

$$N_{VD}(D) = \frac{\int \int \int N_{VD}(x, y, z, D) dx dy dz}{\int \int \int dx dy dz} \tag{9}$$

corresponds to the global PDF of droplet diameters and

$$N_V = \int N_{VD}(D) dD \tag{10}$$

to global DNC.

Ideally, $N_{VD}(x, y, z, D)$ should describe physical reality and it cannot be easily estimated from the measurement just by binning the results (x_i, y_i, z_i, D_i), because due to size-dependent DOF the instrument is able to detect the particle of given size D only inside the limited range of z. If one divides the ranges of the four variables into bins to construct 4-dimensional grid cells, counts entries in each cell and normalizes by cell 4D volumes, then some of the grid cells in such experimentally obtained $N_{VD}^m(x, y, z, D)$ would be intrinsically missing information. For the same reason, the limits of the integral in Eq. (9) along dz should depend on D.

When DSD is concerned, $N_{VD}(D)$ has an advantage over simple PDF since its values can be compared between measurement series. For the same phenomenon, different lens setting should bring the same results. In order to estimate $N_{VD}(D)$, the number of particles within given size range needs to be divided by respective size-dependent volume. Specifically, for the three methods depicted in the previous subsection:

$$N_{VD}^{def}(k) = \frac{M_k}{F \Delta D_k V_k^{def}} \tag{11}$$

$$N_{VD}^{cor}(k) = \frac{M_k}{F \Delta D_k V_k^{cor}} \tag{12}$$

$$N_{VD}^{ind}(k) = \frac{1}{F \Delta D_k} \sum_{i: D_k \leq D_i < D_{k+1}} \frac{1}{V_i^{ind}} \tag{13}$$

where $M_k = |\{i : D_k \leq D_i < D_{k+1}\}|$ is the number of counts within bin k, $\Delta D_k = D_{k+1} - D_k$ is the bin width and F simply the number of frames included in an analysed series.

DSDs obtained with the formulas Eq. (11)-(13) for the laboratory experiment indicate (see Fig. 7) that the values of $N_{VD}(D)$ are significantly underestimated by the default method. It is not surprising, since using Eq. (4) generates SVs which are much larger than the true ones. On the other hand, there is no significant difference between corrected and individual SVs (not shown in the figure). This observation suggests that even without having data for individual droplets usually contained in a particle file, still reasonable DSD can be obtained by correcting accumulated counts listed in a summary file.

Figure 7 compares size distributions of droplets generated with the same device and measured with different lens settings. If each configuration had resolved the whole range of diameters present in a spray, the lines would follow each other. Instead, results approximately agree only for larger droplets which is explained by the instrument resolution improving with the magnification used. The plot suggest that the true minimum droplet size for uniform detection is ∼6 μm for x2 and ∼12 μm for

x1. As expected, those values are greater than 3.7 µm and 6.9 µm, respectively, reported by the producer as the resolution corresponding to the vicinity of the focal plane. Unfortunately, the results do not allow to determine such limit for the lens magnification x4. It can be speculated to equal roughly 4 µm, while definitely stays inside the range defined by the focal plane resolution (about 2 µm) and the above limit for lower magnification (6 µm).
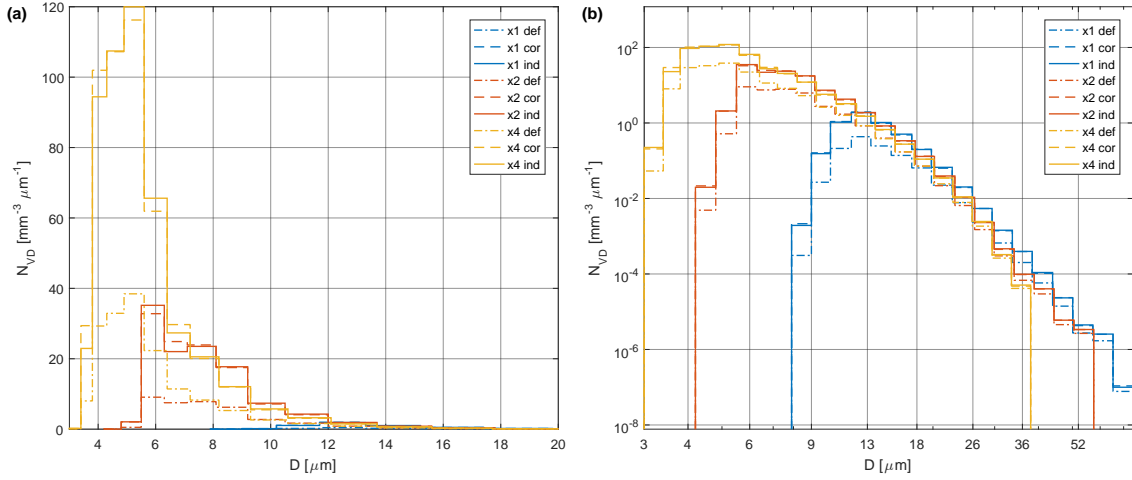
Figure 7. Comparison of droplet size distributions obtained with three methods, default (def), corrected (cor) and individual (ind), in the course of the three measurement series differing in lens magnification settings. Same data plotted in (a) linear and (b) logarithmic scale.

Total DNC N_V can be calculated by suitable integration with respect to the whole range of diameters which in practice turns out into the sum over bins in case of default and corrected method or the sum over individual counts in case of individual method:

$$N_V = \sum_k N_{VD}(k)\Delta D_k \qquad N_V = \frac{1}{F}\sum_i \frac{1}{V_i^{ind}} \qquad (14)$$

Having the information about DNC and DSD, one can calculate simple statistics characterizing the cloud, such as mean droplet diameter $\bar{D}$ or higher order moments of the distribution (mean surface diameter D_2, mean volume diameter D_3, effective diameter D_e). Liquid water content (LWC) can be estimated by summing up volumes of the droplets measured. Because the DSD differs between the methods and lens settings, the resulting mean diameters and LWC will also vary. Table 4 summarizes the results obtained for the poly-disperse stream produced by an ultrasonic generator. DNC is about three to four times larger for corrected and individual method with respect to the default one. In all the cases, statistics of diameter are smaller for new methods in comparison to the default. It can be explained by noting that the largest relative difference in SVs between the methods appears for smallest droplets (see Fig. 5), so it is their contribution to the DSD which changes at most.

Table 4. Results of the laboratory experiment with poly-disperse droplets: comparison of different methods used for estimating size-dependent sample volumes.

Lens setting	x1			x2			x4		
Method	def	cor	ind	def	cor	ind	def	cor	ind
N_V [mm^{-3}]	2.1	8.6	8.6	37.3	112.2	112.3	114.1	331.6	330.1
$\bar{D}$ [µm]	14.1	13.7	13.7	8.3	7.9	7.9	6.0	5.7	5.7
D_2 [µm]	14.5	13.9	14.0	8.6	8.2	8.3	6.4	6.0	6.0
D_3 [µm]	14.9	14.2	14.3	9.1	8.6	8.6	6.9	6.4	6.4
$D_e = D_3^3/D_2^2$ [µm]	15.7	14.9	15.0	10.0	9.4	9.4	8.0	7.3	7.3
LWC [g m^{-3}]	3.6	13.0	13.2	14.5	37.3	37.7	19.6	45.7	46.2

3.5 Homogeneity of detection

275 One of the important properties characterizing particle sizing instrument, apart from the extent of the SV, is homogeneity of detection inside that volume. Perfect homogeneity can be defined as the case when the probability of detecting the given particle of interest is the same everywhere, as long as the particle appears to stand at the position belonging to the respective SV, regardless of how complicated its boundaries are. If the probability depends on the position in space, the results obtained with the system might be biased. It is particularly important for calculating the measures of droplet spatial arrangement, e.g. nearest neighbour distance or radial distribution function (Larsen and Shaw, 2018).

Within the present study, quality of detection is evaluated for shadowgraph system VisiSize D30 based on the long record of the plume of water droplet produced by an ultrasonic droplet generator. As stated earlier (sec. 3.1), the stream of droplets was supposed to extend further than the SV in each direction. Unfortunately, no independent information is available about whether the DNC inside the visible plume was uniform. One can expect that it drops from the maximal value in the center towards the edges where the intensive mixing takes place between cloudy and clear air portions. Nevertheless, the mixing zone was observed to be outside the SV - at least on average, because in general the outflow was quite dynamic. Therefore, statistics integrated over time will be analysed in this section. To allow for drawing conclusions regarding the detection, it is assumed that on average the real physical conditions are homogeneous, i.e. during the experiment the flow filled each part of the entire SV with identical concentration of droplets having identical properties (e.g. DSD).

290 Indeed, results of the experiment integrated over size, time and distance to the focal plane mostly provide relatively constant average droplet concentration with respect to the two principal directions of the camera sensor - horizontal and vertical. The calculated average concentration falls down significantly close to the edges of the FOV (not shown) which is expected concerning border rejection procedure. Figure 8 in panels (a) and (b) shows normalized droplet concentration $N_V(x)/N_V$ and $N_V(y)/N_V$ suitably integrated over size and over other dimensions, divided by the total concentration in order to highlight the

295 relative dependence on position inside the sample volume. The values mostly decrease gradually from the maximum (located left from the center) to the sides in case of horizontal direction and from the bottom to the top in case of vertical. The relative differences, except from very close to the edges, are of the order of 10 %. They are small enough to be possibly caused by the non-uniformities of the plume. The y-dependence of the concentration is more pronounced for larger droplets (above 12 μm, not shown here) which might be the influence of gravity sorting. However, in case of the series recorded with lens setting x1,

300 the concentration falls with height y by a factor of more than 10 from the bottom to the top of the FOV. We speculate this effect is of instrumental origin, as the difference is rather too large (almost exponential) and the timescale too short to allow for the explanation only by gravity sorting of the droplets in the plume. Probable reason is nonuniform illumination of the scene. Although non-uniformities can be compensated for by background normalization (such function is built-in in the software), signal-to-noise ratio of an individual particle shadow might still depend on the position with consequences for detection prob-

305 ability. Due to extensive halo some of the particles might have been rejected. Such problem with illumination might stem from imperfect manual alignment between the laser and the camera, yet we note achieving the satisfactory light conditions with lens setting x1 and lower is challenging. There are no such issues for higher settings, as the FOV is smaller then and it fits easily inside the uniform core of the laser beam.
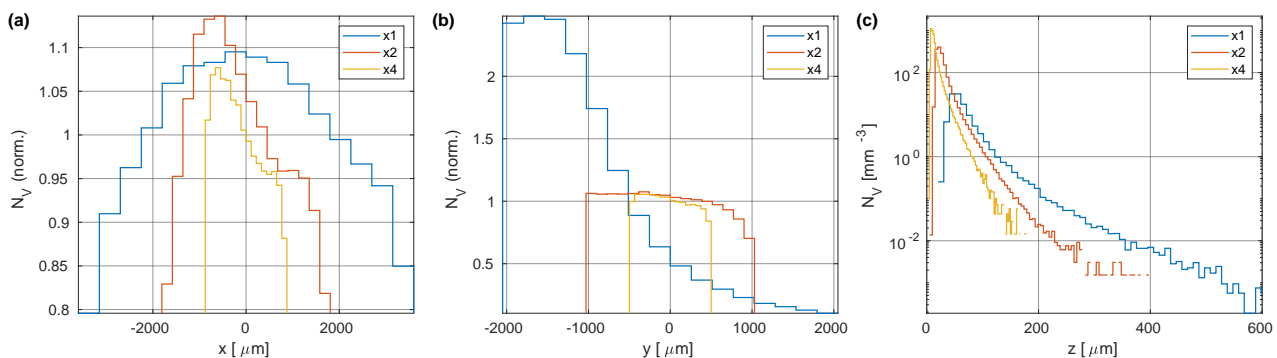
Figure 8. Dependence of droplet concentration on (a) horizontal, (b) vertical and (c) axial position.

Axial dependence is more difficult to evaluate, because the extent of the acceptable DOF depends on both particle size and

310 lens setting. As expected, average concentration decreases with z, since for further distances only the droplets which are large enough can be counted (see Fig. 8 panel (c)). This trend is a result of coexisting effects of DOF limitation and the shape of real DSD where large droplets constitute minor part of the total number. Interestingly, the first z ranges contain a much smaller number of droplets than the maximum located further from the focal plane, regardless of the lens setting. Such unphysical behaviour might stem from the sizing algorithm, which calculates z position out of the halo area. Small particles, like the ones

315 observed in the experiment, are blurred even in the focal plane which makes them being faulty positioned at higher distances than the true ones. Equation (1) assumes no halo for the focal plane $z = 0$ which cannot be realized due to diffraction. Then, non-zero halo A_h is measured and it results in $z > 0$ for all the shadows.

Moreover, it can be noted that for larger distances z the concentration rises with pixel size (falls with magnification, dependent on the lens setting chosen, see Table 1). This fact refers to the DOF limits (Eq. (4)) and respective curves plotted in Fig. 5.

320 Comparison between the three magnifications implies that for any fixed distance z higher than roughly 117 μm, the lower limit of the detectable size range increases with the magnification, i.e. wider spectrum of droplets can be counted at setting x1 than x2 and x4. For example, at $z = 150$ μm, the lens setting x1, x2 and x4 allow for the detection of droplets larger than 21.4, 22.2, 26.4 μm in diameter, respectively.

However, the probability of detection might depend both on the position in space and on the particle size. Therefore, cross-

325 correlated dependence was examined and illustrated in the form of 2-dimensional (z, D) maps in Fig. 9. It is easy to recognize the limitation introduced by the focus rejection criterion which also controls the effective SV (red line). On the other side, the minimum distance z_{min} for a given diameter is well approximated by assuming the halo area in the focal plane equal to the diffraction term ($A_h = \pi D a_5$), analogously to Fig. 4, and solving Eq. (1) for z (blue line).

What is more, the DSD seems to change with the distance z from the focal plane. Precisely, it is a simple consequence of the

330 focus rejection criterion analysed above that the increasing portion of smaller sizes are not detected with increasing distance z but the concentration of sizes which are well above this limit should ideally not change with the distance along the optical axis of the system. In case of lens setting x1, large droplets are present only far from the focal plane and the concentration of droplets of a given size grows with z. Such behaviour suggests that the sizing procedure for the measurement with lens setting x1 might have not work properly. Possibly, due to insufficient brightness of the pictures the halo area was overestimated at the

335 cost of inner particle shadow. According to sizing Eq. (1) and (2), this leads to overestimation of defocus distance together with underestimation of the diameter.
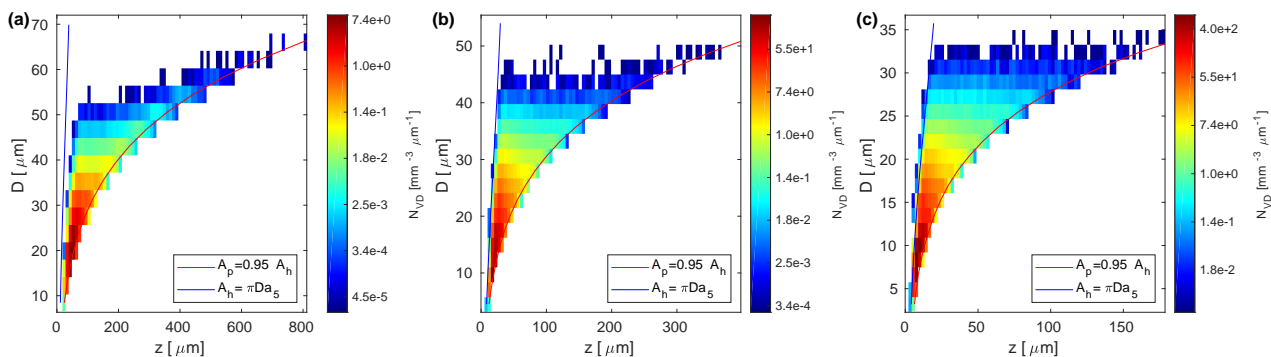
Figure 9. Variability of droplet detection properties in size-space domain for lens setting (a) x1, (b) x2, (c) x4.

As a consequence, the authors discourage using lens setting x1 in further studies of cloud droplets. The large minimum particle size for uniform detection reported earlier (∼12 μm) makes this option of limited utility anyway. Instead, x1 can possibly serve well for the measurements of drizzle drops. In order to avoid the illumination and signal-to-noise issue described

340 above, we would suggest, as a rule of thumb, the lower limit an order of magnitude larger than the effective pixel size (3.69 μm). On the other hand, the objects need to fit into the FOV, so the largest measured size should be a few times smaller than the

shorter dimension (4.1 mm) which eventually results in the conservative range of roughly 40-400 μm. Notwithstanding, so far insufficient data on drizzle has been collected to confirm this expectation experimentally.

In experimental runs with higher magnifications, i.e. lens setting x2 and x4, the (z, D) map features the decrease of concentration with z from the maximum located a bit above z_{min}. The same effect was noticed in Fig. 8 panel (c). Most probably, it relates to the diffraction which is not included in the modeled dependence of the halo area A_h on the diameter D and distance z in Eq. (1). Namely, the equation is not correct in the limit of small z because it implies the object in the focal plane ($z = 0$) should be ideally sharp ($A_h = 0$). Consequently, in this limit the calculated z position is overestimated with respect to the true one. The counts representing droplets standing very close to the focal plane are shifted to the further z-bins in Fig. 9. The extent of this shift is probably not constant but decreases with the true z. Hence, the counts cumulate at some point above z_{min} creating a maximum in $N_V(z)$. We expect the shift to decrease because the calibration constants a_1 and a_2 were fitted by the manufacturer in the procedure resembling Kashdan et al. (2003) so that the Eq. (1) performs satisfactorily in the range of defocus distances and particle diameters typical for industrious applications, i.e. a bit larger than analysed here. Therefore, the estimated z should approach the true one with increasing defocus and droplet diameter.

The shift of the estimated z positions with respect to the true ones is most pronounced in case of the small distances from the focal plane. Importantly, it should have no effect on the accuracy of the sample volume calculation, hence the DNC and the DSD, as long as the z_{95} is not overestimated itself but represents the true distance at which the droplets are no longer counted. We expect this condition to be met if the largest possible defocus z_{95} is significantly higher than the smallest z_{min}. For instance, they differ by a factor of two for diameters larger than 8.0, 6.3, 4.8 μm in case of lens settings x1, x2 and x4, respectively. Those values are close to the minimum diameter for uniform detection estimated in sec. 3.4. It implies the influence on the DSD and the DNC within the valid size range is probably minor. However, we cannot quantify it with high confidence based on the available data.

4 Sizing accuracy

4.1 Diagnostic experiment

Second diagnostic experiment was carried out to characterize instrument performance in terms of particle sizing which affects the relevant statistics of cloud droplets including mean droplet diameter and DSD. Monodisperse water droplets were generated with Flow Focusing Monodisperse Aerosol Generator 1520 (FMAG) manufactured by TSI Inc. and measured with VisiSize D30. FMAG uses periodic mechanical vibration to break a narrow jet of a liquid into droplets of desired size (within the range of 15 to 72 μm in diameter). Efficiency and accuracy of droplet generation is enhanced by aerodynamic flow focusing and charge neutralizer making FMAG a common tool applied for calibration of aerosol spectrometers and droplet sizing instruments (Duan et al., 2016).

In the course of the experiment, pressurized N_2 (1.0 psi) was used as the flow focusing gas, and Ultra-purified H_2O as the liquid. Droplet size was controlled by adjusting two parameters: liquid flow rate and vibration frequency. Three different settings were applied resulting in droplet diameters of 20.13, 39.25 and 57.55 μm as obtained with the formula provided by

the manufacturer (see the settings listed in Table 5). Geometrical standard deviation among the generated droplet population is supposed to be 1.05 or smaller (Duan et al., 2016). The smallest diameter was chosen to ensure relatively narrow spectrum as we observed significant broadening for high vibration frequency which is necessary to generate yet smaller sizes. Presumably, this results in less accurate breakage of the fluid stream or more frequent collisions.

Experimental setup was arranged in two different configurations (see Fig. 10). The first without a cylindrical case over the nozzle, with shadowgraph SV as close as possible to the nozzle head (about 4.5 cm). The second with the case and the dilution air (flow rate of 5 L min^{-1}) forcing the droplets to leave the cylinder. The shadowgraph SV was then located above the cylinder exit (about 18.5 cm over the nozzle head).

Table 5. Settings of the FMAG droplet generator used during sizing tests.

FMAG 1520 settings			
Inlet air [psi]	10.0		
Dilution air [L min^{-1}]	5.0		
Focusing air [psi]	1.0		
Flow rate [mL h^{-1}]	2.0	8.0	18.0
Vibration frequency [kHz]	130	70	50
Droplet size [μm]	20.13	39.25	57.55

4.2 Results

Sample shadow images of droplets produced by the FMAG and captured by the VisiSize D30 are reproduced in Fig. 11. The configuration of the setup was as in panel (c) of Fig. 10, i.e. without the case covering the nozzle. Despite the population of droplets is supposed to be mono-disperse, one can see the range of sizes. For each droplet size specified by the parameters of FMAG, a series of images was taken by the shadowgraph with three different lens magnification settings. Results are presented in Fig. 12 in the form of probability density functions (PDF) (equivalent to $N_{VD}(D)/N_V$). Such measure was chosen in order to compare the DSD between different magnifications and measurements substantially different in total droplet concentration which itself is not quantity of interest in the current analysis.

Strikingly, all the histograms contain multiple peaks which suggests quite frequent collisions between droplets on their way from the nozzle to the SV of the shadowgraph. The position of the first peak corresponds well with the generated droplet size in most of the cases. Its width can be attributed to the inevitable spread of true generated droplet diameters as well as to the imperfect imaging and sizing of droplet shadows. Left-side skewness of the tails suggests partial evaporation. Although in general the effect of evaporation is expected to be more significant for small droplets, the skewness is evident for 39.25 and 57.55 μm measured with the lens settings x1 and x2. We speculate it might be related to the size of the sample volume which increases with the effective pixel size (decreases with magnification) as well as with the particle size (i.e. from the top-left
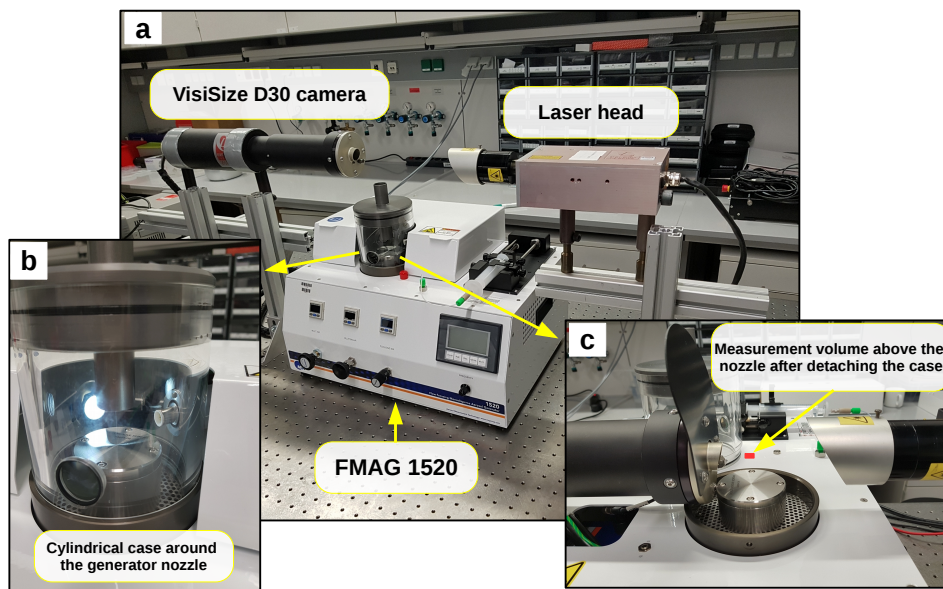
Figure 10. Experimental setup for studying sizing performance: VisiSize D30 located above the exit of FMAG in order to measure outgoing droplets (a) in configuration with the cylindrical case above the nozzle (b) or without it (c).

to the bottom-right panel in Fig. 12). The position of the nozzle exit was adjusted so that the center of the FMAG-generated droplet stream is as close as possible to the focal plane of the shadowgraph. We expect the droplets more distant from the

400 central axis of the stream to be more likely partially evaporated because of the longer travel and exposure to the dry air blown from the area around the nozzle. Those can be detected in case of considerable sample volume but not in case of smaller SV. Importantly, this is only one of the effects which could have contributed to the observed result together with the ambient air properties, velocity of the droplets or some interactions among them.

Taking into account geometric standard deviation of generated droplets (1.05), histogram bin width (0.5 μm) and evaporation,

405 the sizing by shadowgraph is pretty accurate. Only in case of smallest droplets (20.13 μm) and lowest lens magnification (x1) the reported diameters seem to be significantly biased. This issue is probably of instrumental origin and might correspond to non-uniform illumination of the FOV which also caused inhomogeneity of detection of relatively small objects for that particular lens setting (see sec. 3.5).

The fact of droplet collisions is further corroborated with measurements conducted in the configuration as in Fig. 10

410 panel (b), i.e. with the cylindrical case over the nozzle and longer distance between nozzle exit and the shadowgraph SV (around 18.5 cm). Longer path enhances the chance of collisions and effects of evaporation. The former can be clearly seen in
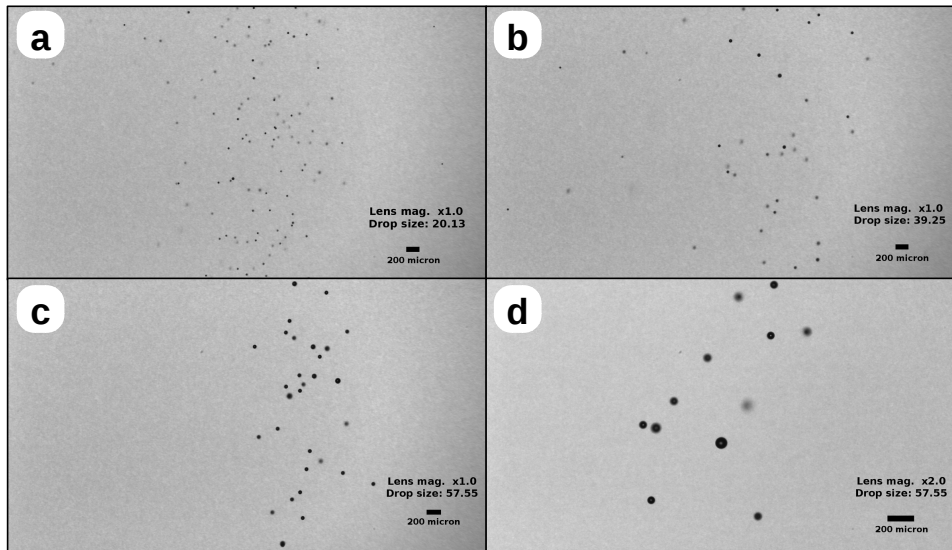
Figure 11. Sample shadow images captured by VisiSize D30 showing droplets of different size generated by FMAG.

histograms presented in Fig. 13. Consecutive peaks correspond to single generated droplet, double collision and triple collision as calculated simply by summing the volumes. Here, lens magnification setting x1 was selected due to largest SV, thus best statistics which can provide better estimation of less frequent events in the probability distribution. More distant peaks can be

415 traced better in case of largest droplet size suggesting the probability of high-order collisions might increase with size. This can be expected recalling extensive studies on cloud droplets collision kernels (Devenish et al., 2012; Grabowski and Wang, 2013). Left-skewed tails are also visible, in particular for the first peak, which is the consequence of evaporation on the way of 18.5 cm from the nozzle.

Finally, the accuracy of sizing is evaluated more quantitatively in the scatter plot in Fig. 14 which compares initial droplet

420 size as specified on FMAG with the results obtained with the shadowgraph – mean droplet diameter reported by the software and the position of the first major peak in the size histogram. Obviously, mean diameter is larger than the first peak as it includes the contribution of collided droplets. Excluding the problematic case of magnification x1 for size 20.13 μm, the position of the first peak deviates up to 2 μm from the original value and the relative error ranges up to roughly 5 %. However, with regard to the accuracy of shadowgraph instrument, it is only an estimation of the upper bound for those quantities, as the generated size

425 is also subject to intrinsic uncertainty. Hence, as far as the comparison with FMAG allows to say, the sizing by shadowgraph is indeed pretty accurate, apart from small droplets observed with magnification x1. Interestingly, the first peak estimation is mostly higher than the FMAG one while the opposite can be expected due to evaporation effects. This fact suggests that the shadowgraph slightly overestimates the sizes in relation to FMAG in most cases.
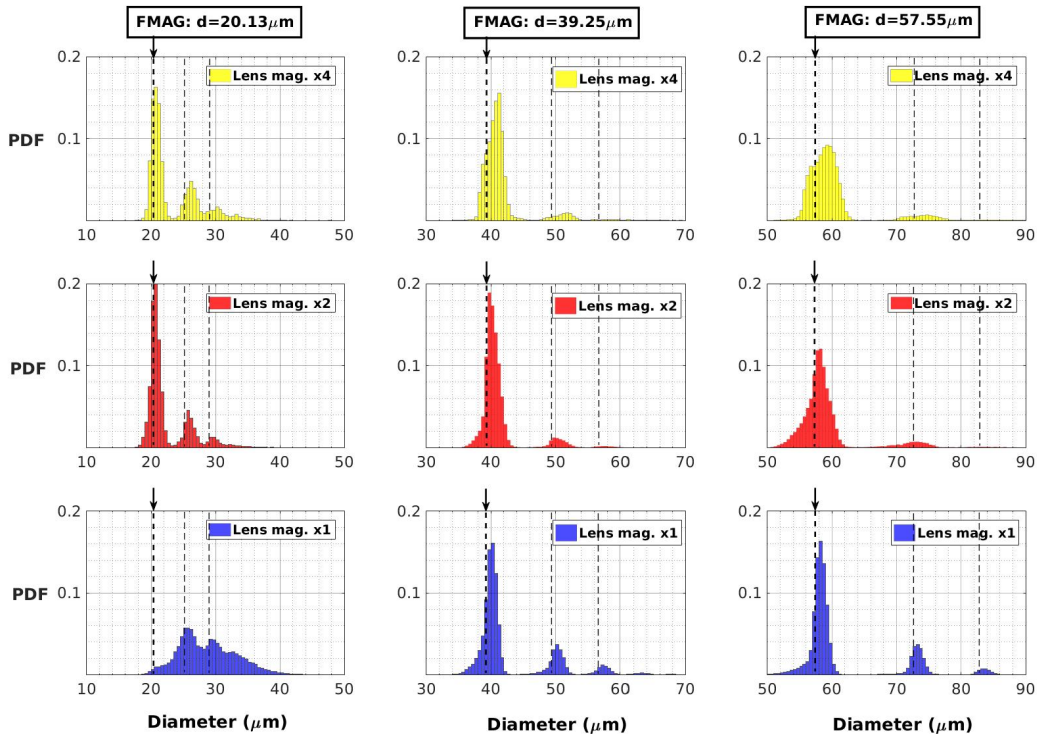
Figure 12. Probability distributions of droplet size measured by VisiSize D30 in configuration as in fig. 10 panel (c) (distance between sample volume and nozzle head is ∼ 4.5 cm), for different camera lens magnifications and different FMAG output droplet sizes. Initial size of the generated droplets as well as the size after double and triple collisions are marked with vertical lines.

5   Field measurements

After laboratory tests, the shadowgraph VisiSize D30 has been used for the first time to measure droplets in atmospheric clouds – in order to test the instrument performance under harsh environmental conditions, compare it with other probes already in service in cloud physics studies, and to study microphysical properties of warm (liquid) orographic clouds. The measurements were performed in a ground-based mountain observatory – Environmental Research Station (Umweltforschungsstation) Schneefernerhaus located on the southern slope of Zugspitze in Bavarian Alps – during two observational periods in July and August 2019. Typical meteorological conditions at this place together with respective cloud and turbulence properties are described in detail by Siebert et al. (2015) and Risius et al. (2015).

Comprehensive analysis of the field experiment alongside with the results obtained with the shadowgraphy imaging technique is going to be covered in a separate article while here we present example observations of cloud microphysical properties representing the range of conditions typical at the place. The data was collected on 13 July 2019 when the clouds covered the sky for most of the day (7-8 oct). However, due to the wind and complex terrain the observatory is usually exposed only to intermittent portions of cloudy air. Two measurements series, each 15 min long, recorded within relatively homogeneous
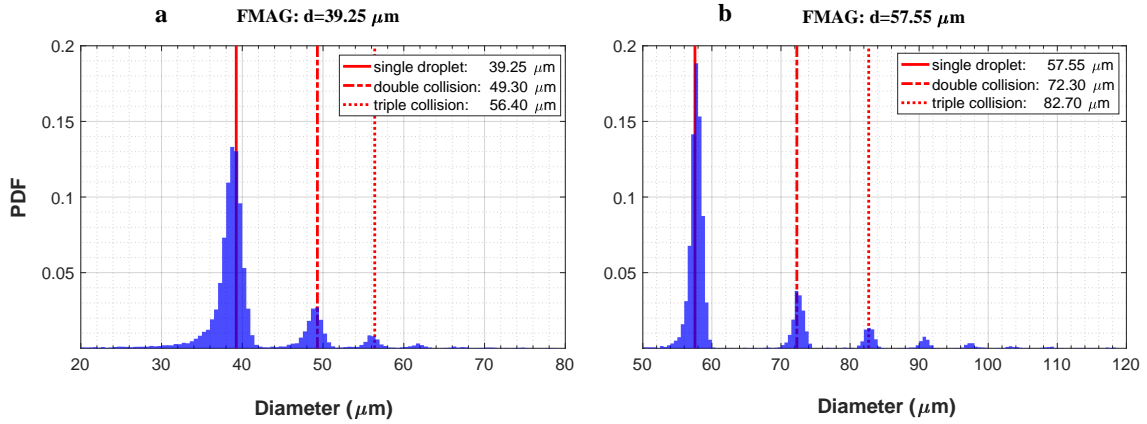
Figure 13. Probability distributions of droplet size measured by VisiSize D30 in configuration as in fig. 10 panel (b) (distance between sample volume and nozzle head is ∼18.5 cm), for camera lens magnification setting x1. Initial size of the generated droplets as well as the size after double and triple collisions are marked with vertical red lines.
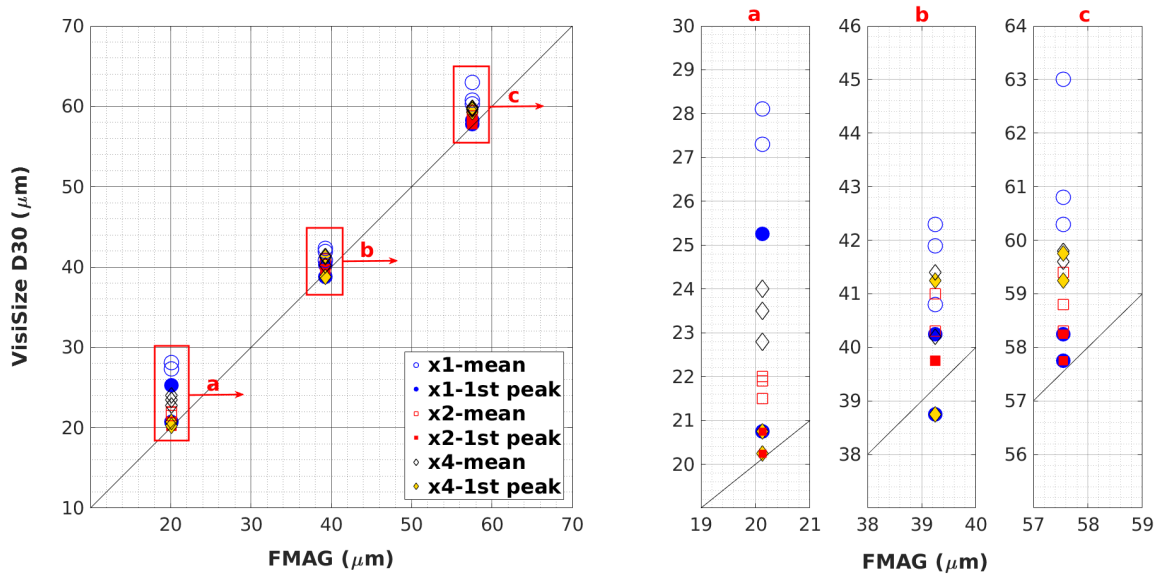
Figure 14. Comparison of droplet sizing between VisiSize D30 and FMAG: scatter plot illustrating the position of the first peak in size histogram and arithmetic mean diameter with respect to FMAG generated droplet sizes for different lens magnification settings (left). Red boxes (a, b, c) are enlarged in panels on the right. Each pair of points (filled and empty) represents a single measurement.

conditions were selected. The first was performed in the afternoon (14:46-15:01 LT) using lens magnification setting x2, the second in the late evening (23:19-23:34 LT) using x4. Throughout the day temperature varied around $0°$ C. Wind was predominantly westerly, coming over the saddle in the mountain range located west from the observatory. It was stronger for the first measurement series, with velocity of around $5 \mathrm{~m\,s^{-1}}$ and fluctuations of $2 \mathrm{~m\,s^{-1}}$, than for the second one (about $1.5 \mathrm{~m\,s^{-1}}$ and $1 \mathrm{~m\,s^{-1}}$ of mean velocity and fluctuations, respectively). There was no precipitation noticed in the afternoon, while light rain occurred in the evening shortly before the measurement.

Figure 15 presents normalized DSDs calculated with the methods described in sec. 3.4 for the two recorded events. Basic microphysical statistics calculated based on the DSDs are listed in Table 6. Naturally, the results cannot be directly compared between the series as the conditions were slightly different. However, DNC as well as mean diameter and LWC resemble typical properties of non-precipitating continental clouds and stay close to the range of conditions reported by Siebert et al. (2015) for Schneefernerhaus observatory based on the measurements with completely different instrument (Phase Doppler Interferometer).
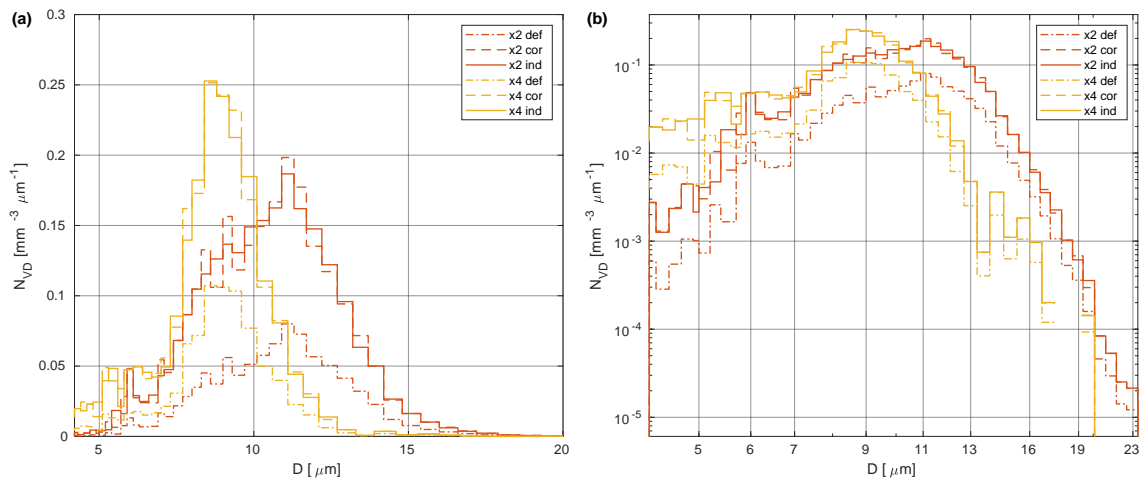
Figure 15. Droplet size distributions observed with the VisiSize D30 in clouds at Schneefernerhaus observatory during two events on 13 July 2019 - afternoon (14:46-15:01 LT) and late evening (23:19-23:34 LT), the former taken with lens setting x2, the latter x4. Three methods of calculating the results are marked with different linestyle: default (def), corrected (cor) and individual (ind) (see sec. 3.4 for explanation). Same data plotted in (a) linear and (b) logarithmic scale.

The cloud observed in the afternoon seems to contain more significant portion of larger droplets (10-15 μm) with respect to the evening one. Yet, in both cases the droplets were produced mostly by condensation as the maximum diameters measured do not correspond to the sizes capable of efficient rain formation by collisions. It should be noted, that moments of the DSD (mean diameter statistics) are most probably moderately overestimated because the portion of small droplets might not be properly detected in the whole relevant volume. This limit of minimum diameter for uniform reliable detection was estimated to be ∼6 μm for lens setting x2 (see sec. 3.4) and unfortunately not found exactly for lens setting x4 (though definitely stays

Table 6. Results of the cloud observations performed with the VisiSize D30 at Schneefernerhaus on 13 July 2019.

Time (Lens setting)	14:46-15:01 LT (mag. x2)			23:19-23:34 LT (mag. x4)		
Method	def	cor	ind	def	cor	ind
N_V [cm^{-3}]	359.4	927.0	928.7	341.6	797.9	797.8
$\bar{D}$ [μm]	10.8	10.6	10.6	9.0	8.8	8.8
D_2 [μm]	11.0	10.8	10.8	9.1	9.0	9.0
D_3 [μm]	11.3	11.0	11.0	9.3	9.1	9.1
$D_e = D_3^3/D_2^2$ [μm]	11.7	11.5	11.4	9.6	9.4	9.5
LWC [g m^{-3}]	0.27	0.65	0.65	0.14	0.32	0.32

between 2 and 6 μm). Obviously, the degree of the bias decreases with magnification (improving resolution). For the same reason, the total DNC might be moderately underestimated with respect to the true one. Nevertheless, all the instruments suffers from similar issues whenever the range of detectable diameters is finite. The relative differences between the three methods of DSD calculation are very similar to what was stated in case of laboratory experiment (sec. 3.4).

The comparison between the two example observations discussed in this section also illustrates the trade-off regarding the choice of magnification. Larger one (x4) provides better resolution and proper representation of the left tail of the DSD (below 6 μm), though the right tail of relatively scarce large droplets is then poorly statistically represented because the total number of counts is quite modest. Specifically, despite the similar DNC and duration of the measurement, roughly 10 times more droplets counts were recorded in the first series (x2), simply due to the larger SV.

6   Conclusions

The shadowgraph imaging system – Oxford Lasers VisiSize D30 – has been tested and characterized with respect to cloud microphysical measurements, i.e. number concentration and size of cloud droplets. The instrument captures images containing shadows of multiple particles, counts them and estimates sizes correcting for image blurring due to out-of-focus position. Although developed for industrial applications, the system can be applied for cloud physics studies. Nevertheless, diagnostic laboratory experiments pointed out important limitations which need to be considered.

First, the sample volume within which a droplet is detectable depends on its size because blurring caused by defocus differently affects images of particles of different size. This fact has to be always taken into account when estimating droplet concentration (in a unit volume). The solution implemented in the software assumes linear relation between depth of field and particle diameter which is efficient for relatively large objects (>260 μm, exact value depends on the lens magnification). However, in case of small droplets, like the cloud ones, additional focus rejection criterion impose much stronger limit on

480 acceptable depth of field. It affects relevant sample volume and leads to underestimated number concentration. Therefore, we developed correction method using sample volume based on that limit.

Second, the analysis of detections in a dense poly-disperse stream of droplets implied that the minimum droplet size for reliably uniform detection is significantly larger than the resolution in the focal plane. It was estimated to be ∼6 μm and ∼12 μm for the camera lens magnification settings x2 and x1, respectively. Potentially, it can be enhanced by careful data

485 conditioning, i.e. with strong limit on the estimated distance from the focal plane, but at the cost of decreasing sample volume. Furthermore, detection probability was found to be satisfactorily homogeneous across the field of view, except for the small magnification setting (x1). Minor issues were revealed with respect to axial direction, probably caused by substantial diffraction effects on small droplets.

Third, the test of sizing accuracy was performed using mono-disperse droplet generator (FMAG 1520, TSI). Substantial

490 effects of droplet collisions and evaporation were observed in the size histograms obtained with the shadowgraph. Notwith-standing, after filtering out collisions by selecting first major peak the results indicated reasonable agreement between diameters reported by the shadowgraph and those supposed to be generated by the FMAG. The relative difference was not larger than 2 μm or 5 %, again except for the lens magnification setting x1 which caused difficulty in uniform illumination of the scene.

Finally, the system under study was applied to sample atmospheric clouds in a ground-based mountain observatory. It per-

495 formed satisfactorily well under windy, cloudy, humid weather conditions and provided quite an extensive set of microphysical data which is intended to be presented and discussed in detail in a separate publication. The results of selected observations analysed here comply with the expected conditions and previous independent measurements performed at that location.

To sum up, the VisiSize D30 can be successfully applied for cloud microphysical measurements. However, relevant quantities like droplet size distribution, number concentration, mean diameter or effective diameter need to be calculated with care,

500 accounting for size-dependent sample volume. While conducting the experiment, one should pay an attention to appropriate adjustments of the laser and the camera in order to assure uniform illumination of the field of view. We recommend to avoid low magnifications (e.g. x1) as they make the proper illumination adjustments more difficult and are of limited utility for cloud studies due to large limit on minimum diameter for satisfactory detection. Those might be instead advantageous for sampling drizzle and rain which is a topic currently under study.

505 *Author contributions.* J.L.N., M.M. and S.P.M. designed the study. J.L.N. planned and carried out the detection experiment (sec. 3). M.M. planned and carried out the sizing experiment (sec. 4). M.M. carried out the field experiment, while M.M. and J.L.N. analysed the collected data. J.L.N. and M.M. wrote the manuscript with contributions from S.P.M.

Competing interests. The authors declare that they have no conflict of interest.

Acknowledgements. We thank Dr. Gholamhossein Bagheri, Dr. Jan Molacek and the staff of Max-Planck Institute for Dynamics and Self-Organisation (MPIDS) for providing FMAG aerosol generator and the help during the sizig laboratory experiments in Goettingen. We are also grateful to Dr. Till Rehm and the staff of Umweltforschungsstation Schneefernerhaus (UFS) for their help during the field measurements at Mt. Zugspitze. Special appreciation is given to Dr. Wojciech Kumala for the technical support in the course of detection laboratory experiments in Warsaw. The authors would like to acknowledge the financial support for this work, provided by the Marie-Sklodowska Curie Actions (MSCA) under the European Union's Horizon 2020 research and innovation programme (grant agreement n°675675).

References

Bachalo, W. D. and Houser, M. J.: Phase/Doppler Spray Analyzer For Simultaneous Measurements Of Drop Size And Velocity Distributions, Optical Engineering, 23, 235 583, https://doi.org/10.1117/12.7973341, 1984.

Barone, T. L., Hesse, E., Seaman, C. E., Baran, A. J., Beck, T. W., Harris, M. L., Jaques, P. A., Lee, T., and Mischler, S. E.: Calibration of the cloud and aerosol spectrometer for coal dust composition and morphology, Advanced Powder Technology, 30, 1805–1814, https://doi.org/10.1016/j.apt.2019.05.023, 2019.

Beck, A., Henneberger, J., Schöpfer, S., Fugal, J., and Lohmann, U.: HoloGondel: in situ cloud observations on a cable car in the Swiss Alps using a holographic imager, Atmospheric Measurement Techniques, 10, 459–476, https://doi.org/10.5194/amt-10-459-2017, 2017.

Bewley, G. P., Saw, E. W., and Bodenschatz, E.: Observation of the sling effect, New Journal of Physics, 15, https://doi.org/10.1088/1367-2630/15/8/083051, 2013.

Bordás, R., Roloff, C., Thévenin, D., and Shaw, R. A.: Experimental determination of droplet collision rates in turbulence, New Journal of Physics, 15, 045 010, https://doi.org/10.1088/1367-2630/15/4/045010, 2013.

Brenguier, J. L., Bourrianne, T., De Coelho, A. A., Isbert, J., Peytavi, R., Trevarin, D., and Weschler, P.: Improvements of droplet size distribution measurements with the fast-FSSP (Forward Scattering Spectrometer Probe), Journal of Atmospheric and Oceanic Technology, 15, 1077–1090, https://doi.org/10.1175/1520-0426(1998), 1998.

Chuang, P. Y., Saw, E. W., Small, J. D., Shaw, R. A., Sipperley, C. M., Payne, G. A., and Bachalo, W. D.: Airborne Phase Doppler Interferometry for Cloud Microphysical Measurements, Aerosol Science and Technology, 42, 685–703, https://doi.org/10.1080/02786820802232956, 2008.

Connolly, P. J., Flynn, M. J., Ulanowski, Z., Choularton, T. W., Gallagher, M. W., and Bower, K. N.: Calibration of the cloud particle imager probes using calibration beads and ice crystal analogs: The depth of field, Journal of Atmospheric and Oceanic Technology, 24, 1860–1879, https://doi.org/10.1175/JTECH2096.1, 2007.

Cooper, W. A.: Effects of Coincidence on Measurements with a Forward Scattering Spectrometer Probe, Journal of Atmospheric and Oceanic Technology, 5, 823–832, https://doi.org/10.1175/1520-0426(1988), 1988.

de Araújo Coelho, A., Brenguier, J. L., and Perrin, T.: Droplet spectra measurements with the FSSP-100. Part I: Low droplet concentration measurements, Journal of Atmospheric and Oceanic Technology, 22, 1748–1755, https://doi.org/10.1175/JTECH1817.1, 2005.

Devenish, B. J., Bartello, P., Brenguier, J. L., Collins, L. R., Grabowski, W. W., Ijzermans, R. H., Malinowski, S. P., Reeks, M. W., Vassilicos, J. C., Wang, L. P., and Warhaft, Z.: Droplet growth in warm turbulent clouds, https://doi.org/10.1002/qj.1897, 2012.

Duan, H., Romay, F. J., Li, C., Naqwi, A., Deng, W., and Liu, B. Y. H.: Generation of monodisperse aerosols by combining aerodynamic flow-focusing and mechanical perturbation, Aerosol Science and Technology, 50, 17–25, https://doi.org/10.1080/02786826.2015.1123213, 2016.

Fugal, J. P. and Shaw, R. A.: Cloud particle size distributions measured with an airborne digital in-line holographic instrument, Atmospheric Measurement Techniques, 2, 259–271, https://doi.org/10.5194/amt-2-259-2009, 2009.

Fugal, J. P., Schulz, T. J., and Shaw, R. A.: Practical methods for automated reconstruction and characterization of particles in digital in-line holograms, Measurement Science and Technology, 20, 75 501, https://doi.org/10.1088/0957-0233/20/7/075501, 2009.

Gerber, H., Frick, G., and Rodi, A. R.: Ground-based FSSP and PVM measurements of liquid water content, Journal of Atmospheric and Oceanic Technology, 16, 1143–1149, https://doi.org/10.1175/1520-0426(1999), 1999.

Glen, A. and Brooks, S. D.: A new method for measuring optical scattering properties of atmospherically relevant dusts using the Cloud and Aerosol Spectrometer with Polarization (CASPOL), Atmospheric Chemistry and Physics, 13, 1345–1356, https://doi.org/10.5194/acp-13-1345-2013, 2013.

Grabowski, W. W. and Wang, L.-P.: Growth of Cloud Droplets in a Turbulent Environment, Annual Review of Fluid Mechanics, 45, 293–324, https://doi.org/10.1146/annurev-fluid-011212-140750, 2013.

Henneberger, J., Fugal, J. P., Stetzer, O., and Lohmann, U.: HOLIMO II: a digital holographic instrument for ground-based in situ observations of microphysical properties of mixed-phase clouds, Atmospheric Measurement Techniques, 6, 2975–2987, https://doi.org/10.5194/amt-6-2975-2013, 2013.

Kashdan, J. T., Shrimpton, J. S., and Whybrew, A.: Two-Phase Flow Characterization by Automated Digital Image Analysis. Part 1: Fundamental Principles and Calibration of the Technique, Particle & Particle Systems Characterization, 20, 387–397, https://doi.org/10.1002/ppsc.200300897, 2003.

Kashdan, J. T., Shrimpton, J. S., and Whybrew, A.: Two-Phase Flow Characterization by Automated Digital Image Analysis. Part 2: Application of PDIA for Sizing Sprays, Particle & Particle Systems Characterization, 21, 15–23, https://doi.org/10.1002/ppsc.200400898, 2004.

Korczyk, P. M., Kowalewski, T. A., and Malinowski, S. P.: Turbulent mixing of clouds with the environment: Small scale two phase evaporating flow investigated in a laboratory by particle image velocimetry, Physica D: Nonlinear Phenomena, 241, 288–296, https://doi.org/10.1016/j.physd.2011.11.003, 2012.

Kumar, M. S., Chakravarthy, S. R., and Mathur, M.: Optimum air turbulence intensity for polydisperse droplet size growth, Physical Review Fluids, 4, 074 607, https://doi.org/10.1103/PhysRevFluids.4.074607, 2019.

Lance, S.: Coincidence errors in a cloud droplet probe (CDP) and a cloud and aerosol spectrometer (CAS), and the improved performance of a modified CDP, Journal of Atmospheric and Oceanic Technology, 29, 1532–1541, https://doi.org/10.1175/JTECH-D-11-00208.1, 2012.

Lance, S., Brock, C. A., Rogers, D., and Gordon, J. A.: Water droplet calibration of the Cloud Droplet Probe (CDP) and in-flight performance in liquid, ice and mixed-phase clouds during ARCPAC, Atmospheric Measurement Techniques, 3, 1683–1706, https://doi.org/10.5194/amt-3-1683-2010, 2010.

Larsen, M. L. and Shaw, R. A.: A method for computing the three-dimensional radial distribution function of cloud particles from holographic images, Atmospheric Measurement Techniques, 11, 4261–4272, https://doi.org/10.5194/amt-11-4261-2018, 2018.

Lawson, R. P., Baker, B. A., Schmitt, C. G., and Jensen, T. L.: An overview of microphysical properties of Arctic clouds observed in May and July 1998 during FIRE ACE, https://doi.org/10.1029/2000JD900789, https://agupubs.onlinelibrary.wiley.com/doi/full/10.1029/2000JD900789https://agupubs.onlinelibrary.wiley.com/doi/abs/10.1029/2000JD900789https://agupubs.onlinelibrary.wiley.com/doi/10.1029/2000JD900789, 2001.

Lloyd, G., Choularton, T., Bower, K., Crosier, J., Gallagher, M., Flynn, M., Dorsey, J., Liu, D., Taylor, J. W., Schlenczek, O., Fugal, J., Borrmann, S., Cotton, R., Field, P., and Blyth, A.: Small ice particles at slightly supercooled temperatures in tropical maritime convection, Atmospheric Chemistry and Physics, 20, 3895–3904, https://doi.org/10.5194/acp-20-3895-2020, 2020.

McFarquhar, G. M., Um, J., Freer, M., Baumgardner, D., Kok, G. L., and Mace, G.: Importance of small ice crystals to cirrus properties: Observations from the Tropical Warm Pool International Cloud Experiment (TWP-ICE), Geophysical Research Letters, 34, https://doi.org/10.1029/2007GL029865, 2007.

Ramelli, F., Beck, A., Henneberger, J., and Lohmann, U.: Using a holographic imager on a tethered balloon system for microphysical observations of boundary layer clouds, Atmospheric Measurement Techniques, 13, 925–939, https://doi.org/10.5194/amt-13-925-2020, 2020.

590 Risius, S., Xu, H., Di Lorenzo, F., Xi, H., Siebert, H., Shaw, R. A., and Bodenschatz, E.: Schneefernerhaus as a mountain research station for clouds and turbulence, Atmospheric Measurement Techniques, 8, 3209–3218, https://doi.org/10.5194/amt-8-3209-2015, 2015.

Rydblom, S. and Thörnberg, B.: Liquid water content and droplet sizing shadowgraph measuring system for wind turbine icing detection, IEEE Sensors Journal, 16, 2714–2725, https://doi.org/10.1109/JSEN.2016.2518653, 2016.

Schlenczek, O.: Airborne and ground-based holographic measurement of hydrometeors in liquid-phase, mixed-phase and ice clouds, Phd
595 thesis, Johannes Gutenberg University in Mainz, https://doi.org/10.25358/openscience-4124, 2017.

Schlenczek, O., Fugal, J. P., Lloyd, G., Bower, K. N., Choularton, T. W., Flynn, M., Crosier, J., and Borrmann, S.: Microphysical Properties of Ice Crystal Precipitation and Surface-Generated Ice Crystals in a High Alpine Environment in Switzerland, Journal of Applied Meteorology and Climatology, 56, 433–453, https://doi.org/10.1175/JAMC-D-16-0060.1, 2017.

Siebert, H., Shaw, R. A., Ditas, J., Schmeissner, T., Malinowski, S. P., Bodenschatz, E., and Xu, H.: High-resolution measurement of cloud
600 microphysics and turbulence at a mountaintop station, Atmospheric Measurement Techniques, 8, 3219–3228, https://doi.org/10.5194/amt-8-3219-2015, 2015.

Woods, S., Lawson, R. P., Jensen, E., Bui, T. P., Thornberry, T., Rollins, A., Pfister, L., and Avery, M.: Microphysical Properties of Tropical Tropopause Layer Cirrus, Journal of Geophysical Research: Atmospheres, 123, 6053–6069, https://doi.org/10.1029/2017JD028068, 2018.